Nanoscale

ROYAL SOCIETY OF CHEMISTRY

PAPER

View Article Online
View Journal | View Issue

Cite this: *Nanoscale*, 2020, **12**, 2532

Intermetallic Pd_3Pb nanocubes with high selectivity for the 4-electron oxygen reduction reaction pathway†

Jocelyn T. L. Gamler,[a] Kihyun Shin,[b] Hannah M. Ashberry,[a] Yifan Chen,[a,c] Sandra L. A. Bueno,[a] Yawen Tang,[c] Graeme Henkelman[b] and Sara E. Skrabalak*[a]

Received 15th November 2019,
Accepted 23rd December 2019

DOI: 10.1039/c9nr09759g

rsc.li/nanoscale

Pd-Based nanoparticles are excellent alternatives to the typically used Pt-based materials that catalyze fuel cell reactions. Specifically, Pd-based intermetallic nanomaterials have shown great promise as electrocatalysts for the oxygen reduction reaction (ORR) in alkaline media; however, their synthesis remains a challenge and shape-controlled nanoparticles are limited. Here, a low-temperature approach to intermetallic Pd_3Pb nanocubes is demonstrated and their electrocatalytic properties evaluated for the ORR. The intermetallic Pd_3Pb nanocubes outperformed all reference catalysts, with a mass activity of 154 mA mg_{Pd}^{-1} which is a 130% increase in activity compared to the commercial Pd/C reference and a 230% increase compared to Pd nanocubes. Tafel analysis reveals that the Pd_3Pb nanocubes are highly selective for the 4-electron reduction pathway, with minimal HO_2^- formation. Density functional theory (DFT) calculations show that the increased activity for the intermetallic nanocubes compared to Pd is likely due to the weakening of OH* adsorption, decreasing the required overpotential. These results show that intermetallic Pd_3Pb nanocubes are highly efficient for the 4-electron pathway of the ORR and could inspire the study of other shape-controlled intermetallics as catalysts for fuel cell applications.

Introduction

Widespread fuel cell use is limited by sluggish reaction kinetics and the high cost of the noble metal electrocatalysts required.[1] Recently, the field has focused on lowering the cost of these catalysts by alloying noble metal nanocatalysts with lower cost and more abundant elements. Alloying can also be used to tune surface electronics, increasing the intrinsic activity.[1] However, the lower-cost element often is removed during long term catalyst usage, which ultimately results in decreased activity. The use of atomically ordered, intermetallic materials with fixed stoichiometry can minimize non-noble metal leaching and provide atomically precise active sites.[2–5] The atomic precision on the surface can allow for enhanced selectivity due to their defined atomic structures and local geometric effects that random alloys do not express.[6–9,10,11] Generally, intermetallics are also more chemically stable than their random alloy counterparts due to lower heats of formation and their regular heteroatomic bonding.[1] Recently we demonstrated that intermetallic cores can be used to stabilize random alloyed surfaces.[12–14] While there is great promise in using intermetallic nanomaterials as catalysts in fuel cells, their synthesis remains challenging. Typical syntheses of these atomically ordered materials involve high-temperature annealing of precursor particles for long periods of time.[15] These harsh reaction conditions lead to polydispersity in particle size and shape, making meaningful structure–function relationships hard to extract. Thus, the synthesis of shape-controlled intermetallic materials is essential to expedite catalyst design.[1,15]

Traditionally, Pt-based nanomaterials are used for both anode and cathode reactions in fuel cells; however, the high cost of Pt and its susceptibility to poisoning motivate the identification of alternative materials. Pd-Based catalysts often offer a lower cost alternative,[16–18] and {100} Pd surfaces and cubic Pd nanocatalysts show superior catalytic activity when compared to Pd nanospheres and {111}-faceted octahedra for several electrochemical reactions, including the oxygen reduction reaction (ORR).[19–23] Recently, intermetallic Pd-based

[a]Department of Chemistry, Indiana University – Bloomington, 800 E. Kirkwood Ave., Bloomington, IN 47405, USA. E-mail: sskrabal@indiana.edu
[b]Department of Chemistry and the Oden Institute for Computational Engineering and Science, The University of Texas at Austin, 105 E. 24th St., Stop A5300, Austin, TX, 78712, USA
[c]Jiangsu Key Laboratory of New Power Batteries, Jiangsu Collaborative Innovation Center of Biomedical Functional Materials, School of Chemistry and Materials Science, Nanjing Normal University, Nanjing 210023, P. R. China

†Electronic supplementary information (ESI) available: Additional characterization of materials by TEM, XRD, STEM, and electroanalytical methods. See DOI: 10.1039/c9nr09759g

nanocatalysts showed both high activities and durability in alkaline media for the ORR.[2,24,25] For example, intermetallic Pd–Pb catalysts showed an 8.8 times increase in activity when compared to a commercial Pd/C catalyst.[26,27] Pd–Pb intermetallic surfaces also show selectivity for the 4-electron reduction pathway and low HO_2^- formation, indicating efficient surface catalysis.[9,26,28] Incorporating Pb into the Pd-based catalysts allow for both strain and ligand effects to enhance the typically sluggish ORR kinetics. Despite their catalytic promise, the synthesis of shape-controlled Pd-based intermetallic nanocatalysts and an understanding of crucial synthetic parameters remains limited.[27,29–31] Here, the synthesis of intermetallic Pd_3Pb nanocubes (NCs) is targeted as catalysts for the ORR *via* a low-temperature colloidal method. These intermetallic NCs also were found to be outstanding, highly efficient catalysts for the ORR as the shape control provided selectivity for the 4-electron pathway.

Experimental

Chemicals

Oleylamine (70%, OLA), oleic acid (OA, 90%) trioctylphosphine (97%, TOP), L-ascorbic acid (L-aa), 1-octadecene (90%, ODE), lead acetylacetonate ($Pb(acac)_2$), palladium(II) bromide ($PdBr_2$) were purchased from Aldrich and unaltered. Perchloric acid solution ($HClO_4$, 1.0 M) was received from Sigma-Aldrich. Nafion (LQ-1105-110 EW at 5%) was purchased from Fuel Cell Store. Nanopure water (18.2 MΩ cm) was used for all electrochemical testing. All chemicals were used without further purification.

Preparation of Pd_3Pb nanocubes

8.2 mg of $Pb(acac)_2$, 19.9 mg of $PdBr_2$, and 38 mg of L-aa were dissolved in a mixture of OLA, OA, and TOP (5.0 mL, 0.5 mL, and 0.5 mL, respectively) in a 8 dram vial with stir bar. The solution was sonicated for 30 min and then added to an oil bath at room temperature. Then the vial and oil bath were allowed to heat up together to 160 °C and incubated for 4 hours. The solution was cooled to room temperature and the particles were precipitated with ethanol and collected by centrifugation. The particles were wash two times with hexane : ethanol mixture (1 : 2) to remove excess organics. The controlled studies were performed in the same manner as described above but the removal of each component in a separate reaction. When OA, TOP, and OLA were removed from the procedure, equal amounts of ODE were added to minimize effects from change in total reaction volume. The Pd_3Pb_1 NP were obtained when both OA and TOP were removed from the reaction procedure and replaced with equal amount of ODE. The Pd nanocubes were synthesize as previously reported.[32] A Branson CPX2800 ultrasonic bath with an output of 110 W and 40 kHz was used for all sonication.

Characterization

All NPs were characterized on JEOL JEM 1010 TEM which operated at 80 keV and images collected with a ROM CCD camera. TEM samples were drop-casted onto the transmission electron microscopy (TEM) grid after the entire sample was washed 2–3 times as described. Additional characterization with scanning transmission electron microscopy-energy dispersive X-ray spectroscopy (STEM-EDX) was completed with JEOL JEM 3200FS operating at 300 keV images taken with Gatan 4k × 4k Ultrascan 4000 camera and the EDX mapping was obtained using and Oxford INCA dispersive X-ray system interfaced with the JEOL JEM 3200FS. The TEM samples were prepared as describe above. The Pd : Pb ratios were determined by using an scanning electron microscope (SEM, FEI Quanta 600F Environmental SEM operating at 30 kV with a spot size of 3) interfaced with an Oxford INCA energy dispersive X-ray detector. These ratios were determined by sampling multiple areas of each sample at low magnification. The power diffraction (XRD) was collected on a PANalytical Empyrean instrument with Cu Kα radiation and an X'Celerator linear strip detector. Rietveld refinement used to determine the XRD fittings with GSAS II.[33] Absorption spectra were obtained using a Cary 100 Bio UV-visible spectrometer with hexane as the solvent. ^{31}P NMR spectra were recorded on a 400 MHz Inova NMR spectrometers. Chemical shifts are reported in ppm on the δ scale relative to the solvent [D_8]-toluene (δ = 2.11 for ^1H NMR) and chemical shifts transferred to the ^{31}P NMR spectra. Fourier-transform infrared spectroscopy (FTIR) spectra were recorded on a Bruker Vertex 70 V FTIR spectrometer in transmission.

Electrochemical evaluation

A Pine Rotating disk electrode (RDE) was used to collect ORR measurements, with AfterMath 1.3.7060 software. A typical three-electrode cell was used where the working electrode was glassy carbon (0.238 cm^2), the reference electrode was Ag/AgCl (4 M KCl), and a graphite rod was used as the counter electrode. All NPs were evenly dispersed on a carbon support (Ketjen EC-600JD). The NPs were massed and then resuspended in 1 mL of hexane. The NPs were then added dropwise to a slurry of the carbon support in 5 mL acetone and 2.5 mL hexane. The mass ratio between the NPs and carbon support was 1 : 1. Once the NPs were added, the solution was sonicated for 1 hour and then left to stir overnight. The solvents were then evaporated and the resulting catalyst dried in vacuum overnight. The working electrode was prepared by creating a 2 mg mL^{-1} ink solution of the catalysts, where the solution consisted of 1 : 3.98 : 0.020 volumetric ratio of isopropanol : H_2O : Nafion. The catalyst ink was sonicated for 30 min and 10 μL was dropcast onto the glassy carbon electrode and dried. The Pd loading was determined by using the metal ratios determined by SEM-EDX in combination with the catalyst preparation method (a 1 : 1 mass ratio of carbon support to nanocatalyst).[13]

Normalization of the electrode by sweeping 200 times between 60 mV and 1200 mV *vs.* RHE was performed first to remove any excess surfactant or surface contamination. Hydrogen desorption experiment were used to determine the electrochemically active surface area (ECSA) and were performed by cycling between 60 and 1000 mV *vs.* RHE in an Ar

purged 0.1 M $HClO_4$ solution. The area under the hydrogen desorption peaks was measured and converted to the active surface area as a common method used throughout the literature giving similar values to those obtained by using the reduction of PdO.[19,21,34,35] The value obtained was then normalized by the Pd loading on the electrode.

Linear sweep voltammetry (LSV) was performed in an O_2-saturated solution of 0.1 M KOH between 60 to 1200 mV (*vs.* RHE) at a scan rate of 10 mV s^{-1} at 1600 rpm. The kinetic current was obtained by collecting LSV curves at several different rotation speeds (400, 900, 1600, 2025, 2500 rpm) and normalized by the mass of Pd to get the mass activity (reproducible within ~20% error). Accelerated durability testing was collected by cycling between 0.6 and 1.0 V *vs.* RHE in O_2-purged 0.1 M KOH 10 000 times. The electron transfer number (n) and % HO_2^- were determined by using rotating ring disk electrode (RRDE) where the disk is glassy carbon and the Pt ring was held at a constant potential of 1.3 V *vs.* RHE and using the equations listed below where I_d is the disk current, I_r is the ring, and N is the current collection efficiency of the Pt ring (0.37).

$$\%HO_2^- = \frac{200I_r}{NI_d + I_r} \quad n = \frac{4NI_d}{NI_d + I_r}$$

Computational methods

GGA-level spin-polarized density functional theory (DFT) calculations were performed with the Vienna *ab initio* simulation package (VASP) using a plane wave basis set with a cut-off energy of 400 eV. The revised Perdew–Burke–Ernzerhof (RPBE) functional was used to describe electron exchange and correlation.[36–38] The Brillouin zone was sampled with a 2 × 2 × 1 *k*-point mesh following the Monkhorst–Pack scheme. The convergence criteria for electronic and geometrical optimization were 10^{-5} eV and 0.01 eV $Å^{-1}$, respectively. We constructed a Pd(100) and intermetallic Pd_3Pb(100) slab systems to model nanocubes having only (100) facets. The slab was constructed by expanding to a 2 × 2 supercell with the bottom two layers fixed in their bulk positions. We considered every possible surface termination and calculated a surface Pourbaix diagram to identify the stable surface configuration with different adsorbates at ORR operating condition. To calculate the ORR activity, the following four associative reaction steps were considered.[39]

$$\Delta G_1: \ O_2(g) + H^+ + e^- + * \ \leftrightarrow \ OOH*$$

$$\Delta G_2: \ OOH* + H^+ + e^- \leftrightarrow \ O* + H_2O(l)$$

$$\Delta G_3: \ O* + H^+ + e^- \leftrightarrow \ OH*$$

$$\Delta G_4: \ OH* + H^+ + e^- \leftrightarrow \ H_2O(l) + *$$

The ORR overpotential was found by a reaction energy diagram, which is drawn with the following equation:[40]

$$\Delta G(U) = \Delta E + \Delta ZPE - T\Delta S + neU$$

where ΔE is the reaction energy, ΔZPE represents the zero-point energy correction, ΔS is the difference in entropy, and U is the applied potential. The chemical potential of the solvated proton and electron pair ($H^+ + e^-$) at standard conditions (p_{H_2} = 1 bar, a_{H^+} = 1, T = 298.15 K) is calculated as $0.5\mu^0_{H_2(g)} - eU$ by assuming equilibrium at the standard hydrogen electrode (SHE).[41,42] Solvation effects, modeled by surrounding the adsorbed species with water molecules, were included in the calculated reaction energy diagrams.[43]

Results and discussion

Shape-controlled Pd_3Pb NCs were synthesized by co-reduction of $PdBr_2$ and $Pb(acac)_2$ with L-aa at 160 °C in a mixture of OLA, OA, and TOP (Fig. 1). These conditions were chosen to facilitate co-reduction of the metal precursors and the selected capping agents (OA and TOP) have been shown to facilitate the growth of the desired nanocubic shape (see ESI† for details).[44,45] The resulting NCs have an average edge length of 9.8 ± 1 nm (Fig. S1†). Powder X-ray diffraction (XRD) of the NCs matches well with the intermetallic Pd_3Pb reference ($Pm\bar{3}m$, ICSD 01-089-2062; Fig. 1B). A high-resolution transmission electron micrograph (HRTEM) of an individual NC shows continuous lattice fringes, indicating single-crystallinity (Fig. 1C). A fast Fourier transform (FFT) of the HRTEM image shows symmetric spots, also supporting the single-crystalline nature of the individual NCs (Fig. 1C, inset). The FFT pattern also indicates that the {200} planes of the cubes are perpendicular to the electron beam and that the NCs are terminated with the expected {200} facets. An interplanar distance of 0.203 nm was obtained from the FFT and corresponds well with the Pd_3Pb expected {200} planes. Scanning transmission electron microscopy (STEM) interfaced with energy dispersive X-ray spectroscopy (EDX) indicates that Pd and Pb are distribu-

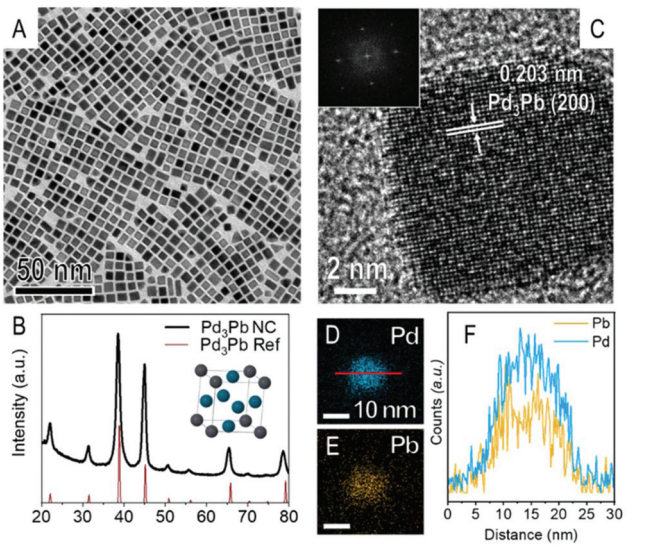

Fig. 1 Characterization of Pd_3Pb NC by (A) TEM, (B) XRD diffraction pattern with a Pd_3Pb reference ($Pm\bar{3}m$, ICSD 01-089-2062) and depiction of the unit cell, (C) HRTEM with inset FFT, and (D and E) STEM-EDX elemental mapping of the NCs and (F) corresponding line scan horizontal across the middle of the particle indicated by the red line in (D).

ted throughout the NC, showing homogeneity of the two elements and roughly the 3 : 1 Pd : Pb ratio (Fig. 1D–F). No phosphorous from the capping ligands was detected by EDX.

To understand how the synthetic conditions facilitate the formation of Pd_3Pb NCs, control experiments were performed in which one reagent was omitted, keeping other synthetic conditions constant to that which produced the NCs shown in Fig. 1; the resulting products were characterized by TEM and XRD (Fig. 2). In the absence of L-aa, a low yield of cubes was observed, with irregularly shaped nanoplates being the major product (Fig. 2A). Nanoplates are typically attributed to slower growth kinetics, which is consistent with the removal of L-aa from the synthesis and leaving OLA as the primary reducing agent.[46] The XRD pattern shows peaks that correspond to the Pd_3Pb phase, but there are also unassigned diffraction peaks and peak broadening that suggest phase impurities (Fig. 2E). Without either OA or TOP, a small yield of cubes is produced but the product consists mostly of ill-defined nanostructures (Fig. 2B and C). Both XRD patterns show the presence of the Pd_3Pb intermetallic phase (Fig. 2E). Without both OA and TOP, small nanoparticles (NPs) with a size of approximately 7 nm were achieved with ill-defined shapes; the XRD pattern matches the intermetallic reference (Fig. S2†). This series of experiments suggest that OA and TOP are central to shape control. When OLA, which can be a weak reducing agent and/or stabilizing agent, was replaced with 1-octadecene, no nanoparticles were isolated and the XRD pattern did not reveal any crystalline phase (Fig. 2D and E). 1-Octadecene is often used as an inert solvent and was used due to its similarity in structure to OLA minus the amine group, which is expected to interact and stabilize the NPs. Taken together, these control experiments demonstrate the importance of all the reagents in the synthesis of Pd_3Pb NCs with high monodispersity. L-aa is important in controlling the reduction to facilitate 3-dimensional growth, and both TOP and OA are important to achieving a high yield of cubes with one crystal phase. Finally, OLA is an important stabilizing agent that keeps the nanoparticles dispersed in solution.

Given the importance of both TOP and OA in achieving a high-quality sample, the OA : TOP ratio was varied in the synthesis while holding other parameters constant. The products were characterized with TEM and Rietveld-refined XRD (Fig. S3–S5†). When the M : OA (where M is the total input metal molar amount) ratio was between 0.06–0.12, a single crystal phase consistent with intermetallic Pd_3Pb was identified (Fig. S4†), with the optimized NC synthesis in terms of nanoparticle size and shape monodispersity having a 0.12 M : OA ratio (Fig. S3B†). When OA is completely removed from the synthesis or the M : OA ratio is too high, phase impurities (*e.g.*, Pd_3Pb_2) appear, which is apparent from the decrease in the percentage of Pd_3Pb phase as revealed from Rietveld refinement (Fig. S4B†). Thus, TOP alone is unable to produce monodisperse NCs. Moreover, when an insufficient amount of TOP is in the synthesis, the yield of cubes is low, with an array of sizes (Fig. S3†). Rather, the M : TOP ratio must be below 0.09, with at least 0.80 mmol of OA to yield a sample with high phase purity. The optimized NC synthesis had a M : TOP ratio of 0.06. Thus, the OA : TOP ratio is crucial for the synthesis of NCs with minimal phase and nanostructure impurities. These observations are unsurprising as both OA and TOP are known to aid in facet expression and can also coordinate directly to the metal precursors to influence the reduction pathway.[44,47–49]

In fact, the product quality was found to be affected by sonication prior to heating, which may be indicative of changes in the local ligand environment of the metal precursors. Specifically, the reaction solution is sonicated (~100 W,

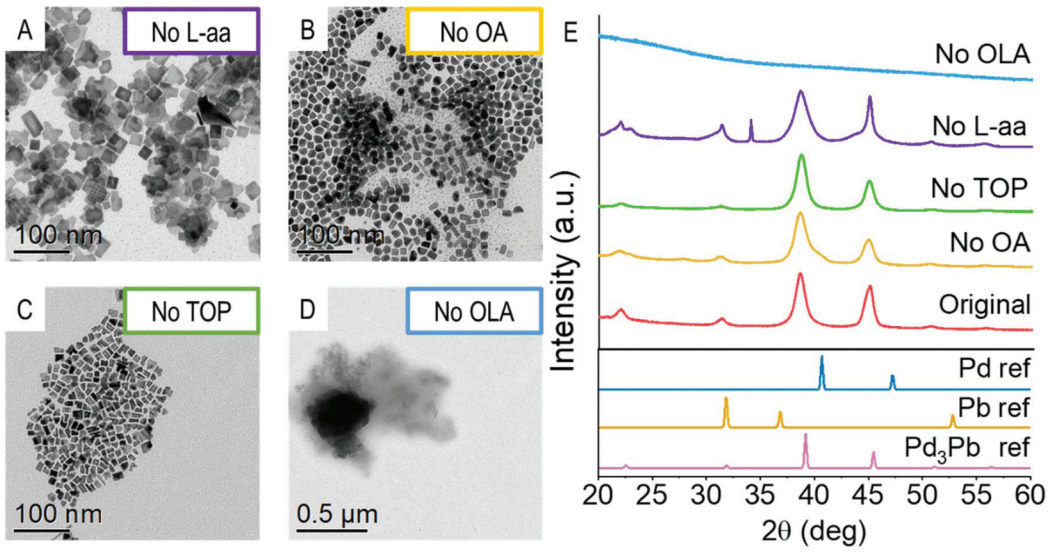

Fig. 2 Characterization of product from control studies, where (A–D) are TEM images of product from when L-aa, OA, TOP, or OLA were omitted, respectively. (E) The corresponding XRD diffraction patterns from the control studies in (A–D) and Pd (ICSD collection code 52251), Pb (ICSD collection code 96501), and Pd_3Pb references (ICSD 01-089-2062).

40 kHz) for 30 minutes prior to heating, but without sonication, the NCs show a large variation in size and sharpness (Fig. S6†). Interestingly, there is little difference in the profile of the UV-visible spectra of the reaction solution before and after sonication, but the solution appears yellow-orange by visual observation before sonication and a deeper orange after sonication (Fig. S7†). These observations suggest that sonication serves to primarily solvate the reagents and facilitate monodisperse growth *via* burst nucleation.[50]

The nature of the metal precursors upon solvation was further probed by UV-visible spectroscopy, NMR, and FTIR, focusing on the interactions of OA and TOP with $PdBr_2$ and $Pb(acac)_2$ as these two reagents contribute to shape- and phase-control (Fig. S8 and S9,† respectively). When $PdBr_2$ is mixed with TOP, the UV-visible spectrum shows a peak around 350 nm, which is consistent with the formation of a Pd–TOP complex as previously reported (Fig. S8A†).[51] This interaction was also confirmed by ^{31}P NMR with the appearance of a new peak at 8.84 ppm, again consistent with literature (Fig. S8B†).[52] UV-visible spectroscopy, NMR, and FTIR were used to study ligand interactions with the Pb center (Fig. S9†). UV-visible spectroscopy shows a change in profile when $Pb(acac)_2$ is mixed with OA and TOP individually (Fig. S9A†). In this case, FTIR can be used to qualitatively understand the Pb–OA interaction as opposed to NMR due to the large amount of protons on the ligand making the NMR spectra difficult to interpret. When OA and $Pb(acac)_2$ are mixed, obvious broadening of the C=O stretch from the carboxylic acid stretching mode around ~1720 cm^{-1} is observed compared to OA by itself; this change is accompanied with the disappearance of the acetylacetonate C=O stretching mode at ~1730 cm^{-1}, which is commonly observed when the acetylacetonate ligand is displaced from a metal (Fig. S9B†).[47] These findings suggest ligand replacement may be occurring with the Pb precursor upon mixing with OA. Interestingly, from the UV-visible spectroscopy experiments, a shift in the lower energy edge from 260 nm to 310 nm is evident when $Pb(acac)_2$ is mixed with TOP; however, ^{31}P NMR did not reveal any additional features or peak broadening consistent with a Pb–TOP complex (Fig. S9C†). These observations suggest that TOP is coordinating with Pd and OA with Pb (but possibly also TOP), which can change the reduction conditions to facilitate the selective synthesis of a single intermetallic phase. The presence of the both TOP and OA are important for achieving the correct pre-nucleation condition to allow for the formation of the intermetallic phase. Cooperatively, TOP and OA are also crucial capping agents that facilitate the formation of NCs.

With the synthetic parameters central to formation of phase- and shape-controlled samples identified, the performance of the Pd_3Pb NCs as an electrocatalyst for the ORR was evaluated (Fig. 3). This work was motivated, in part, by recent studies suggesting that incorporation of Pb into the Pd lattice can lead to enhanced selectivity for the 4-electron pathway of the ORR due to tensile strain imparted to Pd surfaces.[9,26–28] Moreover, {100}-terminated Pd NCs have slightly higher activity than {111}-terminated Pd octahedra for the ORR, making our Pd_3Pb NCs a promising nanocatalyst and an excellent platform for elucidating the roles of composition and shape to performance.[22,23,53] Specifically, the Pd_3Pb NCs were evaluated for the ORR and compared to Pd_3Pb NPs with an ill-defined morphology (Fig. S2†), Pd NCs (Fig. S10†), and a commercial Pd reference (Fuel Cell Store, 20 wt% Pd) (see ESI† for details).

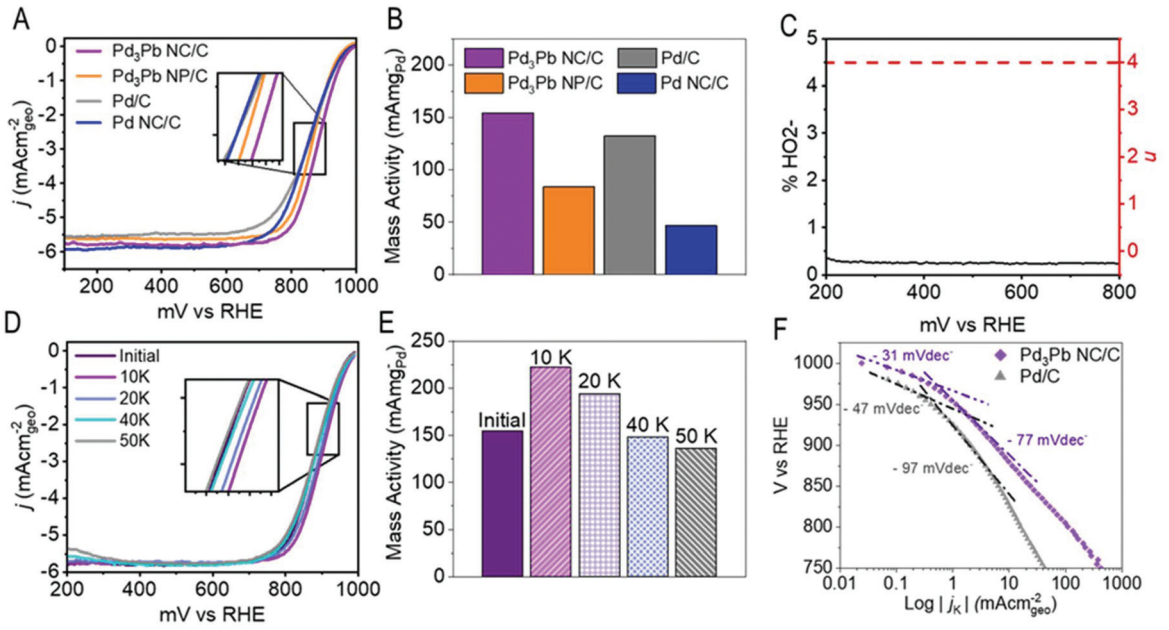

Fig. 3 (A) Polarization curves collected in O_2-saturated 0.1 M KOH and (B) corresponding mass activities. (C) RRDE results for the determination of % HO_2^- and *n* for Pd_3Pb NC/C. (D) Polarization curves collected in O_2-saturated before and after ADT and (E) mass activities after ADT at different intervals for the Pd_3Pd NC/C. (F) Tafel plots for Pd_3Pb NC/C compared to the Pd/C.

The Pd_3Pb NPs synthesized without TOP and OA (Fig. S2†) serve as a good comparison structure to elucidate the importance of shape-control and the Pd NCs (Fig. S10,† average edge length 10 nm) are a good reference to understand the influence of composition. All nanoparticles were deposited onto a carbon support (Ketjen EC-600JD) for testing and are denoted as Pd_3Pb NC/C, Pd_3Pb NP/C, Pd NC/C, and Pd/C (Fig. S11†). The electrochemical surface area (determined by cyclic voltammograms collected in Ar-purged 0.1 M $HClO_4$) for the Pd_3Pb NC/C is larger than all other tested catalysts (Fig. S12†). Polarization curves were collected in O_2-saturated 0.1 M KOH and the mass activities were determined using the Koutecky–Levich method (Fig. 3).[54] The half-wave potential ($E_{1/2}$), often used as a qualitative way to evaluate activity, for the Pd_3Pb NC/C (880 mV *vs.* RHE) is shifted +15 mV more positive when compared to Pd_3Pb NP/C (865 mV). The $E_{1/2}$ for both Pd–Pb catalysts are shifted more positive than Pd NC/C (860 mV) and Pd/C (860 mV) references. The initial mass activities (kinetic current (I_k) normalized by the Pd loading) show that the Pd_3Pb NC/C have significantly higher activity than all other tested catalysts. The activities for the four catalysts are Pd NC/C < Pd_3Pb NP/C < Pd/C < Pd_3Pd NC/C (Fig. 3B). The Pd_3Pb NC/C gave a 230% increase when compared to the Pd NC/C reference and an 84% increase when compared to the smaller Pd_3Pb NP/C. The enhanced performance of Pd_3Pd NC/C compared to Pd NC/C highlights the importance of the intermetallic composition. The importance of shape is evident from the comparison of Pd_3Pd NC/C to Pd_3Pb NP/C, with Pd_3Pb NP/C having decreased activity consistent with its non-cubic shape; however, we note that the decreased activity may also arise from decreased ordering, which was qualitatively evaluated by comparing the relative intensities of the superlattice and fundamental XRD peaks.[8]

A rotating ring-disk electrode at 1600 rpm and Pt ring held at 1.3 V *vs.* RHE was used to determine the electron transfer number (n) and the percentage of peroxide formed. The n was determined to be approximately 3.92, demonstrating that the ORR favors the 4 e^- route on the Pd–Pb intermetallic surface (Fig. 3C). The Pd_3Pb NC/C also show a low percentage of HO_2^- formation (<1%), indicating high catalytic efficiencies for the complete reduction of oxygen (Fig. 3F). Tafel plots also were obtained for each catalyst in two potential windows (high potential, low current and low potential, high current; Fig. 3F and Fig. S13†). The Tafel slopes for the Pd_3Pb NC/C are lower than all other tested catalysts. In the high potential region, the Tafel slope for the Pd_3Pb NC/C was −31 mV dec^{-1}, which is obviously lower than −47 mV dec^{-1} Pd/C reference as well as the other two tested catalysts (−49 mV dec^{-1} for Pd_3Pb NP/C and −64 mV dec^{-1} for Pd NC/C). The lower Tafel slopes for the cubic intermetallic catalyst indicates the outstanding electrocatalytic reaction kinetics.[55] The high activity for the Pd_3Pb NC/C catalysts and the high efficiencies suggest good ORR reaction kinetics for the shape-controlled intermetallic catalyst.

To probe the origin of the catalytic enhancement provided by Pd_3Pb NC/C compared to the references, DFT was used to determine the overpotential for the ORR on the $Pd_3Pb(100)$ and Pd(100) surfaces (Fig. 4). Several surface terminations for Pd(100) and $Pd_3Pb(100)$ slabs were calculated to identify the most stable structure under basic conditions. Considering the space group $Pm\bar{3}m$, $Pd_3Pb(100)$ has two different terminations: one with alternating Pd and Pb atoms and the other terminated with only Pd atoms. The surface energies of the different terminations are summarized in Fig. S14.† When the intermetallic slab was terminated with Pd atoms, a surface reconstruction occurred with local regions of both (100) and (111) character, consistent with what has been observed for NPs.[56,57] The Pd termination on the intermetallic slab with this surface reconstruction was found to be the most stable with a surface energy of 0.0486 eV $Å^{-2}$; this surface was used as the model for subsequent adsorption calculations (Fig. S14c†). We attempted to deform the pure Pd(100) slab to the same reconstructed surface structure with mixed (100) and (111) regions, but the

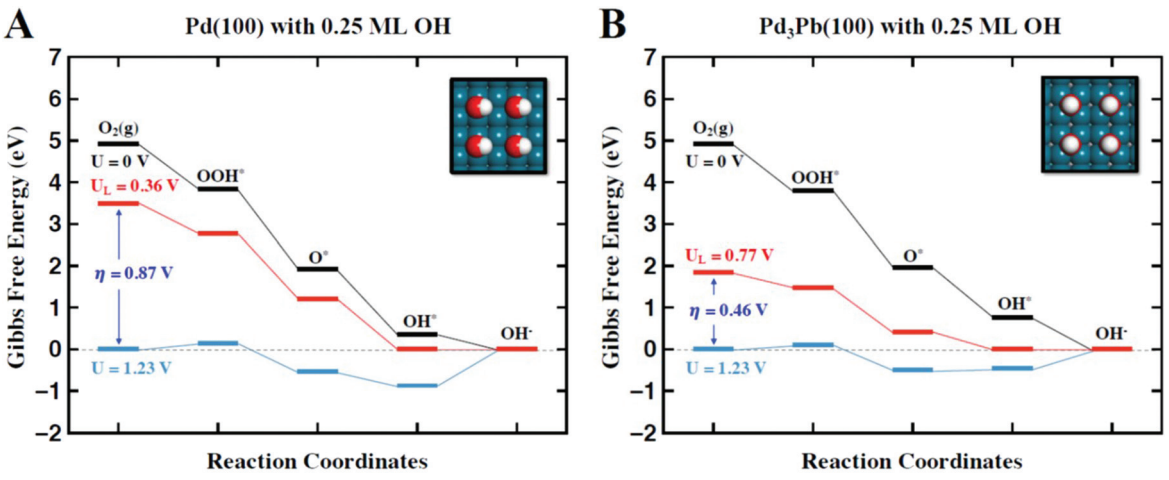

Fig. 4 Plots of Gibbs free energy *versus* the reaction pathway for (A) Pd(100) and (B) $Pd_3Pb(100)$ surface with 0.25 ML hydroxide where the U_L (red) indicates the limiting potential and η indicates the overpotential ($\eta = 1.23 - U_L$). Here, the $Pd_3Pb(100)$ surface has a Pd termination. This coverage was used to calculate the overpotential for the ORR.

surface relaxed back to the unreconstructed (100) surface upon geometric optimization.

Under ORR conditions, the surface of the catalyst can be covered with adsorbates, causing changes in the activity. To find the most stable surface under ORR reaction conditions, the surface Pourbaix diagram was calculated as a function of applied potential (Fig. S15†). Surfaces with 0.25 ML of the O* and OH* intermediates were considered on both the Pd(100) and Pd_3Pb(100) surfaces. Both diagrams show similar trends: the bare surface is stable at potentials below 0.4 V, 0.25 ML OH* is stable between 0.4 and 1.1 V, and 0.25 ML O* is stable above 1.1 V. According to our experimental results, ORR occurs between 0.7–0.9 V. In this potential range, 0.25 ML hydroxide is stable on both Pd(100) and Pd_3Pb(100), so this coverage was used to calculate the overpotential for the ORR. The reaction energy diagram and overpotential on the optimized Pd(100) and Pd_3Pb(100) surfaces as determined by the surface stability and Pourbaix diagram calculations. The binding energy of each intermediate (O*, OH*, and OOH*) was calculated for the associative ORR mechanism to produce the reaction energy diagrams in Fig. 4. Each figure has three graphs, corresponding to different potentials. The energy diagram calculated at the limiting potential (U_L, red trace in Fig. 4) is the most important because the limiting potential represents the highest potential where no reaction step is endothermic. A higher limiting potential corresponds to a lower overpotential and a higher catalytic activity. Fig. 4A shows that the rate-determining step for Pd(100) is the final step corresponding to the release of OH*. On Pd(100), the binding of OH* is too strong so that bound OH* becomes an inhibitor for the generation of OH^-. Bound OH* on the Pd_3Pb(100) surface also inhibits formation of OH^- (Fig. 4B), but the OH* binding energy is weaker than on Pd(100) by 0.41 eV. This difference in OH* binding energy for the Pd_3Pb(100) surface results in a corresponding decrease in the overpotential of 0.41 V. For comparison, the overpotential for ORR on the Pd(100) surface is 0.87 V. Weaker OH* binding on Pd_3Pb(100) arises from the different surface terminations (shown in Fig. S14 and S15B†). Generally, OH* prefers to bind on top or bridge sites;[58] however, in our calculations, OH* binds at four-fold hollow sites on the Pd_3Pb(100) surface. On monometallic Pd(100) and (111) surfaces, the bond length between nearest neighbor Pd atoms is 2.75 Å. On Pd_3Pb(100), before the surface reconstruction, the Pd–Pd bond is longer (2.85 Å) than on Pd(100), and it becomes even longer (2.97 Å) after reconstruction. This long bond length results in a different stable OH* binding site, and to the significantly different binding energies of OH*, which directly affects the difference in overpotential between Pd(100) and Pd_3Pb(100). We also calculated the ORR overpotential on bare Pd(100) and Pd_3Pb(100) surfaces without pre-adsorbed OH* and found that Pd_3Pb(100) is still a better ORR catalyst than Pd (100) (see Fig. S16†).

Given the high efficiency of the Pd_3Pb NCs, accelerated durability testing (ADT) was used to evaluate whether or not this high performance could be maintained with time. The potential was cycled between 600 and 1000 mV *vs.* RHE for 10 000 times in O_2-saturated 0.1 M KOH and the ORR activity was measured afterward. The Pd_3Pb NC/C show a +15 mV shift in the $E_{1/2}$, whereas Pd_3Pb NP/C shows a −15 mV shift (Fig. 3D and Fig. S17†). In fact, the Pd_3Pb NC/C showed a 53% activity increase after 10 000 cycles. In contrast, the Pd_3Pb NP/C showed a 43% decrease and the commercial Pd/C a 7% decrease (Fig. S18†). TEM analysis of the used catalysts show that the three references suffer from significant aggregation and particle morphology changes, which can account for the lack of particle stability over extended cycling (Fig. S19†). STEM-EDX mapping for the Pd_3Pb NP/C used catalyst showed the formation of large aggregations (Fig. S20†). In the case of Pd_3Pb NC/C, STEM-EDX elemental maps suggest formation of a Pd-rich exterior after the initial 10 000 cycles, with Pd-rich exteriors having been shown to be a more active catalyst configuration in some bimetallic systems (Fig. 5).[27] It is clear that there is a change in the nanoparticle morphology after the first 10 000 cycles resulting in rounding of the initial cubic shape and is discussed further below. Bulk measurements by EDX to determine the Pd : Pb ratio before and after ADT for these two samples were recorded (Fig. S20B† and Fig. 5I). EDX was used as opposed to ICP-MS due to the minimal amount of catalysts recovered from the electrode after electrochemical testing. There is a small change in the ratio after ADT for the Pd_3Pb NC/C catalysts, suggesting minimal metal leaching from the cubic intermetallic arrangement as there are also minimal changes in particle size. The Pd_3Pb NP/C sample showed larger changes in the atomic ratios after 10 000 cycles, indicating that there is more leaching of the Pb from the surface of the catalyst suggesting a lack of stability of the ill-defined nanostructures.

The positive shift in the $E_{1/2}$ and activity increase for the Pd_3Pb NC/C indicates that the surface is more active than before the first 10 000 potential cycles. One explanation could be from a change in morphology correlating with a change to more intrinsically active reaction sites. However, additional analysis suggests that the catalytic efficiencies, *i.e.*, the selectivity for the preferred 4-electron pathway, are better on the initial catalytic surface and that the enhanced activity is due to a change to a less efficient mechanism. This assertion is based on the calculation of electron transfer number and % HO_2^- determined by RRDE. Thus, when the n and % HO_2^- were calculated after 10 000 and after 50 000 cycles, there is a significant decrease in the n and a large increase in the % HO_2^- formation when compared to the initial values (Fig. S21†). This finding indicates that even after the first 10 000 cycles where we observed an increase in activity, there is a decrease in the selectivity and efficiency of the surface catalysis; thus, the nanocubic Pd_3Pb catalyst is beneficial for improving the selectivity of the ORR.

This change in mechanism after the first 10 000 cycles could arise from structural changes and slight Pb removal from the surface to create a Pd rich exterior, which as previously mentioned has been shown to have excellent ORR activities in alkaline media.[27] When durability testing is continued for the Pd_3Pb NC/C catalysts, there are small negative

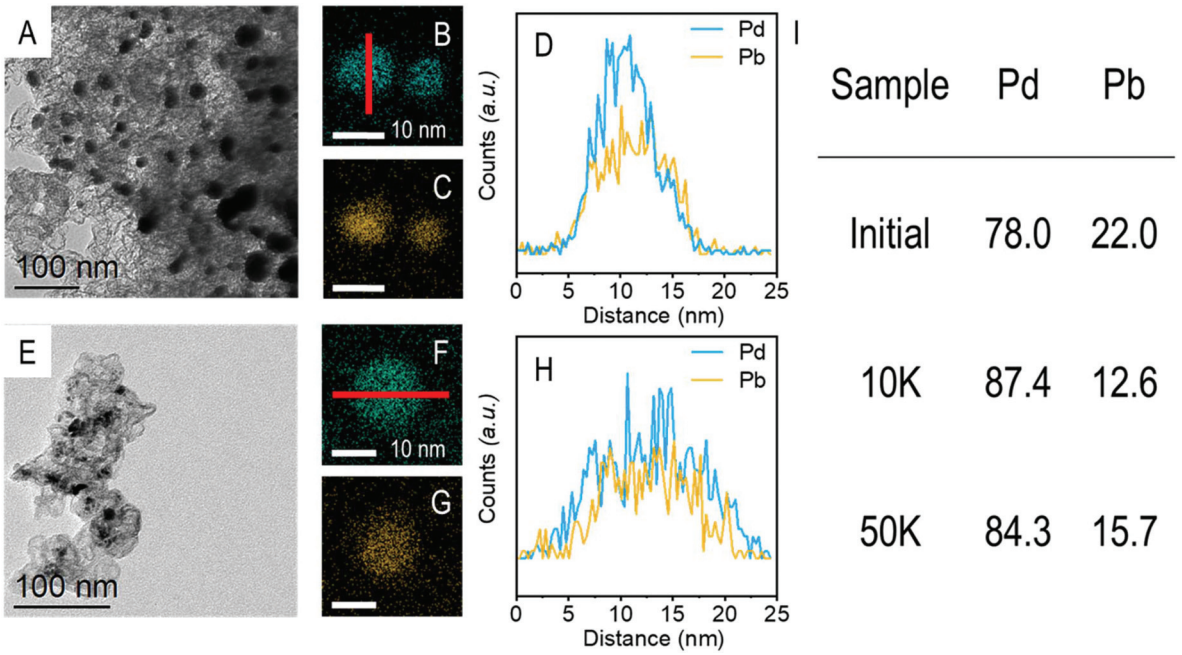

I

Sample	Pd	Pb
Initial	78.0	22.0
10K	87.4	12.6
50K	84.3	15.7

Fig. 5 Post stability characterization for Pd_3Pb NC/C catalysts after (A–D) 10 000 cycles and (E–H) after 50 000 cycles by (A and E) TEM, (B and C) and (F and G) STEM-EDX elemental maps and (D and H) elemental line scans indicated by the red line in B and F. (I) The atomic percentage determined by EDX of the initial catalyst, after 10 000 cycles, and after 50 000 cycles.

shifts in the $E_{1/2}$ until it reaches the initial value (Fig. 3D). After 50 000 cycles the activity only shows a 12% decrease from the initial starting point. After the 10 000 cycles there is a decrease in the ECSA and then thereafter minimal changes in the cyclic voltammogram profiles collected in Ar-purged 0.1 M $HClO_4$ indicating minimal changes in the ECSA after 10 000 cycles (Fig. S22†). The small shifts in the $E_{1/2}$ and small changes in the activities after extended ADT demonstrate the use of shape-controlled Pd_3Pb NC/C serving as superior ORR catalysts with long lifetimes. The used catalysts were also characterized after 50 K cycles and it is clear there is more particle deformation possibly from aggregation (Fig. 5). STEM-EDX shows that after 50 000 cycles the Pd-rich exterior is still present. With the characterization after ADT and the extensive electrochemical testing, the Pd_3Pb NC/C were found to be superior nanocatalysts when compared to all other catalysts tested in terms of both catalytic activity and durability. One can imagine coating the shape-controlled intermetallic NPs to preserve the cubic shape and maintain the superior selectivity for the 4-electron pathway.[59]

Conclusions

In summary, we have demonstrated a low-temperature synthesis of shape-controlled intermetallic Pd_3Pb NCs. We have also demonstrated the importance of each reagent in the successful creation of the shape-controlled intermetallics, where the TOP : OA ratio is extremely important for achieving monodisperse and single-phase nanoparticles. These shape-controlled Pd_3Pb NCs showed high activity when compared to three other Pd-based references. The kinetics of the ORR on the shape-controlled intermetallic nanoparticle showed high efficiencies, with low formation of HO_2^- and an n close to 4. Computational results suggest the catalytic enhancement for the Pd_3Pb surface results from a weakening in the binding energy of OH* when compared to the Pd(100) surface, resulting in a lower overpotential. These results show great promise for the advancement of catalyst development by moving towards shape-controlled intermetallic nanoparticles for fuel cell applications. We also imagine exchanging Pb for another less toxic metal, decreasing the risk of leaching Pb into the environment. We have shown that the intermetallic NCs have high catalytic efficiencies in terms of electron transfer number and low byproduct formation, thus it would be of interest to better preserve the shape through the use of additional coatings that would be permeable enough to allow for the ORR catalysis but stable enough to not allow surface diffusion or particle aggregation.

Conflicts of interest

There are no conflicts to declare.

Acknowledgements

S. E. S, J. T. L. G., H. M. A., and S. L. A. B. acknowledge financial support from Indiana University and U.S. DOE BES Award DE-SC0018961 for support of material synthesis, characterization, and catalytic evaluation. Access to the powder diffract-

ometer was provided by NSF CRIF CHE-1048613. We also want to thank the IU Electron Microscopy Center and Nanoscale Characterization Facility for access to the necessary instrumentation. The calculations by K. S. and G. H. were supported by the Welch Foundation (F-1841) and the Texas Advanced Computing Center. Assistance and analysis of catalytic results by Y. C. and Y. T. was supported by the National Natural Science Foundation of China (No. 21875112), National and Local Joint Engineering Research Center of Biomedical Functional Materials and Priority Academic Program Development of Jiangsu Higher Education Institutions. Y. C. also thanks China Scholarship Council (Grant No. 201806860028) for the award of a fellowship. S. L. A. B thanks NSF DGE-1342962 for the Graduate Research Fellowship.

References

1 J. T. L. Gamler, H. M. Ashberry, S. E. Skrabalak and K. M. Koczkur, *Adv. Mater.*, 2018, **30**, 1801563.
2 E. Antolini, *Appl. Catal., B*, 2017, **217**, 201–213.
3 D. Wang, H. L. Xin, R. Hovden, H. Wang, Y. Yu, D. A. Muller, F. J. DiSalvo and H. D. Abruña, *Nat. Mater.*, 2013, **12**, 81–87.
4 N. Hodnik, C. Jeyabharathi, J. C. Meier, A. Kostka, K. L. Phani, A. Rečnik, M. Bele, S. Hočevar, M. Gaberšček and K. J. J. Mayrhofer, *Phys. Chem. Chem. Phys.*, 2014, **16**, 13610–13615.
5 Y. Kang, J. B. Pyo, X. Ye, T. R. Gordon and C. B. Murray, *ACS Nano*, 2012, **6**, 5642–5647.
6 W. Xiao, W. Lei, M. Gong, H. L. Xin and D. Wang, *ACS Catal.*, 2018, **8**, 3237–3256.
7 Y. Pei, Z. Qi, T. W. Goh, L.-L. Wang, R. V. Maligal-Ganesh, H. L. MacMurdo, S. Zhang, C. Xiao, X. Li, F. (Feng) Tao, D. D. Johnson and W. Huang, *J. Catal.*, 2017, **356**, 307–314.
8 D. Kim, C. Xie, N. Becknell, Y. Yu, M. Karamad, K. Chan, E. J. Crumlin, J. K. Nørskov and P. Yang, *J. Am. Chem. Soc.*, 2017, **139**, 8329–8336.
9 Q. Shi, C. Zhu, C. Bi, H. Xia, M. H. Engelhard, D. Du and Y. Lin, *J. Mater. Chem. A*, 2017, **5**, 23952–23959.
10 L. Bu, C. Tang, Q. Shao, X. Zhu and X. Huang, *ACS Catal.*, 2018, **8**, 4569–4575.
11 L. Bu, Q. Shao, Y. Pi, J. Yao, M. Luo, J. Lang, S. Hwang, H. Xin, B. Huang, J. Guo, D. Su, S. Guo and X. Huang, *Chem*, 2018, **4**, 359–371.
12 C. Wang, X. Sang, J. T. L. Gamler, D. P. Chen, R. R. Unocic and S. E. Skrabalak, *Nano Lett.*, 2017, **17**, 5526–5532.
13 J. T. L. Gamler, A. Leonardi, H. M. Ashberry, N. N. Daanen, Y. Losovyj, R. R. Unocic, M. Engel and S. E. Skrabalak, *ACS Nano*, 2019, **13**, 4008–4017.
14 J. T. L. Gamler, H. M. Ashberry, X. Sang, R. R. Unocic and S. E. Skrabalak, *ACS Appl. Nano Mater.*, 2019, **2**, 4538–4546.
15 Y. Yan, J. S. Du, K. D. Gilroy, D. Yang, Y. Xia and H. Zhang, *Adv. Mater.*, 2017, **29**, 1605997–1616059.
16 M. Shao, P. Liu, J. Zhang and R. Adzic, *J. Phys. Chem. B*, 2007, **111**, 6772–6775.
17 M.-H. Shao, K. Sasaki and R. R. Adzic, *J. Am. Chem. Soc.*, 2006, **128**, 3526–3527.
18 M. V. Castegnaro, W. J. Paschoalino, M. R. Fernandes, B. Balke, M. C. M. Alves, E. A. Ticianelli and J. Morais, *Langmuir*, 2017, **33**, 2734–2743.
19 H. Erikson, A. Sarapuu, N. Alexeyeva, K. Tammeveski, J. Solla-Gullón and J. M. Feliu, *Electrochim. Acta*, 2012, **59**, 329–335.
20 C.-L. Lee, H.-P. Chiou and C.-R. Liu, *Int. J. Hydrogen Energy*, 2012, **37**, 3993–3997.
21 F. J. Vidal-Iglesias, R. M. Aran-Ais, J. Solla-Gullon, E. Garnier, E. Herrero, A. Aldaz and J. M. Feliu, *Phys. Chem. Chem. Phys.*, 2012, **14**, 10258–10265.
22 S. Kondo, M. Nakamura, N. Maki and N. Hoshi, *J. Phys. Chem. C*, 2009, **113**, 12625–12628.
23 M. Shao, J. Odell, M. Humbert, T. Yu and Y. Xia, *J. Phys. Chem. C*, 2013, **117**, 4172–4180.
24 G. Fu, Y. Liu, Z. Wu and J.-M. Lee, *ACS Appl. Nano Mater.*, 2018, **1**, 1904–1911.
25 E. Meku, C. Du, Y. Sun, L. Du, Y. Wang and G. Yin, *J. Electrochem. Soc.*, 2016, **163**, F132–F138.
26 Z. Cui, H. Chen, M. Zhao and F. J. DiSalvo, *Nano Lett.*, 2016, **16**, 2560–2566.
27 C. Tang, N. Zhang, Y. Ji, Q. Shao, Y. Li, X. Xiao and X. Huang, *Nano Lett.*, 2019, **19**, 1336–1342.
28 A. J. Jeevagan, T. Gunji, F. Ando, T. Tanabe, S. Kaneko and F. Matsumoto, *J. Appl. Electrochem.*, 2016, **46**, 745–753.
29 J. Zhang, W. Xu, L. Xu, Q. Shao and X. Huang, *Chem. Mater.*, 2018, **30**, 6338–6345.
30 C. Tang, N. Zhang, Q. Shao, X. Huang and X. Xiao, *Nanoscale*, 2019, **11**, 5145–5150.
31 H. Xu, P. Song, C. Fernandez, J. Wang, M. Zhu, Y. Shiraishi and Y. Du, *ACS Appl. Mater. Interfaces*, 2018, **10**, 12659–12665.
32 M. Jin, H. Liu, H. Zhang, Z. Xie, J. Liu and Y. Xia, *Nano Res.*, 2011, **4**, 83–91.
33 B. H. Toby and R. B. Von Dreele, *J. Appl. Crystallogr.*, 2013, **46**, 544–549.
34 M. Hara, U. Linke and Th. Wandlowski, *Electrochim. Acta*, 2007, **52**, 5733–5748.
35 X. Huang, S. Tang, X. Mu, Y. Dai, G. Chen, Z. Zhou, F. Ruan, Z. Yang and N. Zheng, *Nat. Nanotechnol.*, 2011, **6**, 28–32.
36 J. P. Perdew, K. Burke and M. Ernzerhof, *Phys. Rev. Lett.*, 1996, **77**, 3865–3868.
37 J. P. Perdew, K. Burke and M. Ernzerhof, *Phys. Rev. Lett.*, 1997, **78**, 1396–1396.
38 B. Hammer, L. B. Hansen and J. K. Nørskov, *Phys. Rev. B: Condens. Matter Mater. Phys.*, 1999, **59**, 7413–7421.
39 H. A. Hansen, J. Rossmeisl and J. K. Nørskov, *Phys. Chem. Chem. Phys.*, 2008, **10**, 3722–3730.
40 J. K. Nørskov, J. Rossmeisl, A. Logadottir, L. Lindqvist, J. R. Kitchin, T. Bligaard and H. Jónsson, *J. Phys. Chem. B*, 2004, **108**, 17886–17892.
41 V. Viswanathan, H. A. Hansen, J. Rossmeisl and J. K. Nørskov, *ACS Catal.*, 2012, **2**, 1654–1660.

42 A. A. Peterson, F. Abild-Pedersen, F. Studt, J. Rossmeisl and J. K. Nørskov, *Energy Environ. Sci.*, 2010, **3**, 1311–1315.
43 S. Liu, M. G. White and P. Liu, *J. Phys. Chem. C*, 2016, **120**, 15288–15298.
44 J. Zhang and J. Fang, *J. Am. Chem. Soc.*, 2009, **131**, 18543–18547.
45 J. Li, F. Li, S.-X. Guo, J. Zhang and J. Ma, *ACS Appl. Mater. Interfaces*, 2017, **9**, 8151–8160.
46 Y. Xiong, I. Washio, J. Chen, H. Cai, Z.-Y. Li and Y. Xia, *Langmuir*, 2006, **22**, 8563–8570.
47 S.-W. Kim, J. Park, Y. Jang, Y. Chung, S. Hwang, T. Hyeon and Y. W. Kim, *Nano Lett.*, 2003, **3**, 1289–1291.
48 N. Ortiz, R. G. Weiner and S. E. Skrabalak, *ACS Nano*, 2014, **8**, 12461–12467.
49 N. Ortiz and S. E. Skrabalak, *Angew. Chem., Int. Ed.*, 2012, **51**, 11757–11761.
50 Y. Xia, Y. Xiong, B. Lim and S. E. Skrabalak, *Angew. Chem., Int. Ed.*, 2009, **48**, 60–103.
51 Z. Yang and K. J. Klabunde, *J. Organomet. Chem.*, 2009, **694**, 1016–1021.
52 S. U. Son, Y. Jang, K. Y. Yoon, E. Kang and T. Hyeon, *Nano Lett.*, 2004, **4**, 1147–1151.
53 M. Shao, T. Yu, J. H. Odell, M. Jin and Y. Xia, *Chem. Commun.*, 2011, **47**, 6566–6568.
54 S. Liu, X. Mu, H. Duan, C. Chen and H. Zhang, *Eur. J. Inorg. Chem.*, 2017, **2017**, 535–539.
55 T. Shinagawa, A. T. Garcia-Esparza and K. Takanabe, *Sci. Rep.*, 2015, **5**, 13801.
56 D. F. Yancey, L. Zhang, R. M. Crooks and G. Henkelman, *Chem. Sci.*, 2012, **3**, 1033–1040.
57 J. H. Ryu, S. S. Han, D. H. Kim, G. Henkelman and H. M. Lee, *ACS Nano*, 2011, **5**, 8515–8522.
58 H. Li, K. Shin and G. Henkelman, *J. Chem. Phys.*, 2018, **149**, 174705.
59 Y. Hu, K. Tao, C. Wu, C. Zhou, H. Yin and S. Zhou, *J. Phys. Chem. C*, 2013, **117**, 8974–8982.